Nanotechnology

ACCEPTED MANUSCRIPT

Etched ion tracks in amorphous SiO_2 characterised by small angle X-ray scattering: influence of ion energy and etching conditions

To cite this article before publication: A Hadley *et al* 2019 *Nanotechnology* in press https://doi.org/10.1088/1361-6528/ab10c8

Etched ion tracks in amorphous SiO_2 characterised by small angle X-ray scattering: influence of ion energy and etching conditions

A. Hadley[1], C. Notthoff[1], P. Mota-Santiago[1], U. H. Hossain[1], N. Kirby[2], M. E. Toimil-Molares[3], C. Trautmann[3,4] and P. Kluth[1]

[1]*Department of Electronic Materials Engineering, Research School of Physics and Engineering, Australian National University, Canberra ACT 2601, Australia*

[2]*Australian Synchrotron, ANSTO, 800 Blackburn Rd Clayton VIC 3168, Australia*

[3]*GSI Helmholzzentrum für Schwerionenforschung, Plankstr. 1, Darmstadt 64291, Germany*

[4]*Technische Universität Darmstadt, Darmstadt 64289, Germany*

Abstract

Small angle X-ray scattering was used to study the morphology of conical structures formed in thin films of amorphous SiO_2. Samples were irradiated with 1.1 GeV Au ions at the GSI UNILAC in Darmstadt, Germany, and with 185, 89 and 54 MeV Au ions at the Heavy Ion Accelerator Facility at ANU in Canberra, Australia. The irradiated material was subsequently etched in HF using two different etchant concentrations over a series of etch times to reveal conically shaped etched channels of various sizes. Synchrotron based SAXS measurements were used to characterise both the radial and axial ion track etch rates with unprecedented precision. The results show that the ion energy has a significant effect on the morphology of the etched channels, and that at short etch times resulting in very small cones, the increased etching rate of the damaged region in the radial direction with respect to the ion trajectory is significant.

1. Introduction

Biological cellular membranes contain naturally occurring nano-scale ion channels which sense and control the translocation of ions and molecules across cell walls [1]. They have been used successfully to detect the artificial translocation of molecules through pores, however they suffer from limited chemical and thermal stability as well as the limitation of fixed diameters of the pores. Pores in solid state materials such as silicon dioxide (SiO_2) and silicon nitride (Si_3N_4) provide a robust alternative with the potential of being able to be integrated into standard electronic device processing [1]. Artificial pores also possess added versatility enabling functionalisation for specific applications by the control of size and surface properties [2-4], leading to promising applications such as sensors and in novel nano-fluidic and electronic devices [5, 6].

The "ion track etching" technique is an industrially compatible method that can be used to generate nano-scale pores in a variety of materials including polymers, minerals, and the insulators SiO_2 and Si_3N_4 which are commonly used in semiconductor processing. A major advantage of the ion track etching method is that pores generated using this method may be tailored to suit a wide variety of applications. In industry the technique is used for the fabrication of ion track etched porous membranes in thin polymer foils with many applications including filtration, particle separation, chemical and biological sensing [1, 7], and as templates for nanowire and nanotube synthesis [8].

Various other methods have been used to generate nano-scale pores in a variety of materials. For example, electron beam lithography and anisotropic etching can be used sequentially to fabricate pores with diameters of around 20 to 200 nm in very thin membranes. Subsequent electron beam processing can reduce the diameter of a single pore to around 5 nm [9]. Single holes may also be drilled into thin membranes using focussed ion beam sculpting techniques as demonstrated by Li *et al.* [10]. Conical pores of aspect ratio around 5:1 have been fabricated in Si by directed self-assembly of block copolymers (polystyrene-b-polymethylmethacrylate, PS-b-PMMA) [11, 12] and in SiO_2.[13], however these pores are not randomly distributed, and they have relatively wide size distributions and surface roughness inside the pore walls. Using the ion track etching technique it is possible to create just one single pore [14, 15], or as many as are required by control of the ion fluence. The ion track etching method does not require expensive dedicated lithography systems as in the methods described in [9, 10]. The pores are randomly distributed, highly uniform, and parallel with very high aspect ratios (can be >1000:1 in some materials) and have very narrow size distributions. The morphology of the etched ion tracks can be tailored for specific applications by choice of etching and irradiation conditions resulting in cylindrical, cigar-shaped, conical or double conical etched channels [8].

Ion track etching is based on the preferential dissolution of damaged material left in the wake of a swift heavy ion, as first observed in lithium fluoride crystals by Young in 1958 [16]. Several models have been developed to explain the formation of ion tracks, and a recent review which discusses some of these models and their limitations is given in [17]. A commonly accepted and useful simple model is the thermal spike model [18, 19], which assumes that as a swift heavy ion passes through a solid, energy is transferred, primarily triggering excitation and ionization processes. Via the resulting electron cascade the deposited energy is radially distributed with respect to the ion trajectory and a fraction of this energy is finally transferred to the atomic lattice via electron-phonon coupling. The temperature of the target material can increase above the melting point along a narrow region around the ion trajectory which subsequently re-solidifies very quickly into a permanently damaged region, or so-called "ion track". A mathematical representation of the model often takes the form of two coupled heat diffusion equations, each related to the time scale of their individual process. Criticisms of the thermal spike model have been that it does not adequately represent the time scales of the relevant processes, and that non-thermal effects are not represented. Several theoretical studies have dealt with these issues by using a combination of numerical analysis and molecular dynamics simulations [20-22]. However, although the thermal spike model is a simple model, when used in conjunction with molecular dynamics simulation, it can yield valuable results that agree well with experiments [23, 24].

In many materials, the damaged ion track region is more susceptible to chemical etching than the undamaged material introducing a local etch anisotropy which can be used to produce uniform pores with extremely small minimum openings. (For example see Siwy *et al.* [25], who estimated by conductivity measurements that the small opening of conical structures in the polymer polyethylene terephalate (PET) was just a few nanometers.) For uniform preferential etching to occur along the length of the ion track a material-dependent electronic stopping power must be exceeded [26].

Although polymer etched ion track membranes have been commercially produced for many years and many studies on their fabrication and characterisation have been conducted, the transition into commercial applications for nanopores fabricated in SiO_2 and Si_3N_4 by the ion track etching method has been less successful, despite the fact that the mechanisms for track formation are well understood [19, 23, 27, 28]. Reliable and reproducible production of pores in these materials is highly desirable since they exhibit mechanical, chemical and thermal stability under a wide range of conditions, including those used to fabricate semiconductor devices. They provide a more robust alternative to polymer membranes, but their fabrication is more challenging due to the chemical environments needed to produce them [3]. Accurate characterisation of the etched tracks is also difficult due to their

size and the possibility of the introduction of artefacts due to sample preparation and characterisation techniques.

Track etching in SiO_2 has previously been studied by several groups, for example see [29-31]. In each of these studies irradiation with a range of ion energies below and above the threshold for continuous etching was conducted, with a focus on the energy threshold required for uniform etching. The main measure for consistent track etching in all three cases was the uniformity of the base cone radii at the surface of the samples observed by scanning electron microscopy (SEM) or atomic force microscopy (AFM). Dallanora *et al.* [29] used transmission electron microscopy (TEM) cross-section images to compare the cone opening angles generated by etching tracks irradiated with low ion energies. Milanez *et al.* [31] also compared the radii of the etched pits at the surface measured using AFM and cross-sectional TEM, finding that for deep holes of around 75 nm the cone radii measured using both techniques did not match. Because the structures resulting from etching ion tracks can be very narrow and deep, the AFM probe tip radius may have been too large to fit inside the narrow channel, causing distortion in the results as was also observed by Vlasukova *et al*. [32]. While microscopy techniques can be useful for characterisation of etched structures, the sample preparation is tedious and may adversely affect the resulting image. For sufficient statistics many samples must be prepared (for example see [3]) to be sure a representative population of etched structures has been considered. In particular, none of the studies cited above were able to accurately determine the cone opening angles. To date in the literature on ion track etching in SiO_2, there has been no systematic approach to study the dependence of the etch pit morphology upon etchant concentration and irradiation conditions. Here, we present a systematic study of the etching behavior of ion tracks in thermally grown amorphous SiO_2 (a-SiO_2). The issues mentioned above are addressed in the present study by the use of small angle X-ray scattering (SAXS) as the main characterisation technique, supported by SEM imaging and analysis. SAXS does not require any sample preparation and does not introduce any artefacts that can influence the measurement results. It is very difficult to accurately measure the dimensions of the cones by SEM, as that would require the individual preparation of exact cross-sectional samples for each cone. SAXS has proven to be well suited to characterise both un-etched and etched ion tracks [28, 33-35]. It enables us to leverage statistics by simultaneously measuring many structures at once (around 2×10^6 for an ion fluence of 1×10^8 ions cm^{-2} and an X-ray beam spot size of 220 x 100 μm^2), providing statistical information on the etched track morphology over the entire track length [36]. This cannot be achieved using microscopy, however the direct SEM images agreed very well with the indirect SAXS measurements, supporting our choice of model for data analysis and verifying our SAXS measurement method. Due to the extremely narrow size distribution of the structures resulting from ion track etching, the averaged value results are representative of the

individual pores. We used SAXS to determine the track etch rates in both the radial and axial directions as a function of etching and irradiation parameters. This technique provides a far more accurate method to characterise the ion track etching process in a-SiO_2 than has been achieved previously.

2. Experimental details

2.1. Pore formation

Commercially obtained 2 μm thick a-SiO_2 films thermally grown on <100> Si wafer substrates were irradiated with 1.1 GeV Au ions at the UNILAC accelerator at GSI in Darmstadt, Germany, and with 185, 89 and 54 MeV Au ions at the ANU Heavy Ion Accelerator Facility in Canberra, Australia. Figure 1 shows a plot of the energy loss of Au ions in a-SiO_2 calculated using SRIM 2008 [37]. The energy loss values plotted are for Au ions entering the layer at the surface. At the ion energies studied, electronic stopping is the primary means for transfer of energy to the sample, and the nuclear stopping is negligible. The average electronic stopping power values across a 2 μm layer of SiO_2 for each energy studied are given in Table 1.

Low irradiation fluences in the order of 10^8 to 10^9 ions cm^{-2} were chosen to minimise the probability of overlap of the etched tracks. Samples were subsequently etched at room temperature in hydrofluoric acid (HF) diluted to concentrations of 5% and 2.5%, for a series of etching times between 1 to 12 minutes. To stop the etching process, each sample was rinsed in deionised water and allowed to dry in air. Samples were studied using synchrotron based small angle X-ray scattering and scanning electron microscopy. SEM images were collected using an FEI Verios scanning electron microscope. The samples were imaged with no additional conductive coating so as not to obscure any fine features. Figure 2 is an SEM micrograph showing the conical shape of etched ion tracks in SiO_2. Figure 2(a) is a cross-sectional view of etched ion tracks in SiO_2 irradiated with 5 x10^8 cm^{-2} 185 MeV Au ions and etched in 5% HF for 8 minutes. The conical shape of the etch pits can clearly be observed, with two cones shown in cross-section at the centre of the image. The smaller V-shape at the top of the left cone is a partially overlapping cone behind the cone at the front of the sample. Figure 2(b) shows a plan view of the top of the sample surface showing that the etched tracks are randomly distributed with minimal overlap and the openings are of very uniform size.

2.2. Small angle X-ray scattering

SAXS measurements were conducted at the SAXS/WAXS beamline of the Australian Synchrotron in Melbourne, Australia. They were performed in transmission configuration with a photon energy of 12 keV and a camera length of approximately 7.2 m. Images were collected with a 2-dimensional Pilatus 1M hybrid pixel detector using exposure times between 0.5 to 5 seconds. Calibration with a silver behenate (AgBeh) standard was used to accurately determine the camera length for the experimental set-up for each group of measurements. Samples were mounted on a three-axis goniometer, enabling accurate alignment with the incident X-ray beam. Samples were aligned with the X-ray beam as accurately as possible by tilting the sample in three directions to obtain a concentric scattering pattern as shown in the top left image of Fig. 3. Measurements were performed by tilting the samples by an

angle γ with respect to the X-ray beam and scattering images collected for each tilt angle for a tilt sequence from 0° up to 50° in increments of 5°. The relative accuracy of the tilting angle γ was better than $\pm 0.1°$ corresponding to the smallest increment of the stepper motors. This means that if there is a small offset in the initial alignment with the X-ray beam, it will persist through the complete tilt sequence and it can be determined by fitting the images obtained from multiple tilt angles. Figure 3 shows a SAXS measurements of a tilt sequence from 0° to 40° with the experimentally obtained scattering patterns on the left. As the tilt angle is changed from 0° the scattering image becomes non-isotropic with the appearance of two crossing streaks. As the tilt angle is increased, the angle between the streaks changes.

The scattering intensity $I(\vec{q})$ recorded by the 2-D detector resembles an interference pattern which occurs as a result of changes in the electron density within the sample. It can be expressed as a function of the scattering vector $\vec{q}$ where $\vec{q}$ is the difference between the incident X-ray beam and the scattered beam as shown in Fig. 4. The magnitude of $\vec{q}$ is related to the scattering angle 2θ by

$$|q| = \frac{4\pi sin\theta}{\lambda} \qquad (1)$$

where λ is the wavelength of the incident X-ray beam. For randomly arranged scattering objects with minimal overlap, the scattering intensity $I(\vec{q})$ can be expressed as

$$I(\vec{q}) \propto N \Delta\rho |f(\vec{q})|^2 \qquad (2)$$

where $\Delta\rho$ is the density contrast between the reduced density of the etched ion tracks and the surrounding a-SiO_2, N is the number of scattering objects and the modulus of $f(\vec{q})$ is the scattering amplitude. Mathematically the scattering amplitude, or form factor, is essentially a Fourier transform of the three-dimensional variation in electron density [38].

To model the experimental data, we have to assume an appropriate model for $f(\vec{q})$. Conical-shaped objects are an appropriate choice for the model as is apparent from the SEM image in Fig. 2. The geometry of the more simple case of a cylinder is given in [39]. The reference frame we choose for our real space objects (the cones) is the axis of the cone, shown by the dotted line in Fig.4. We assume the cones are radially symmetric about the axis and model them using cylindrical coordinates as shown in Fig. 4, where H is the height of the cone, β is the half cone opening angle and R is the radius at the base of the cone. The form factor for a cone of height H and base radius R can be expressed as

$$f(q_r, q_z) = \int_0^H \int_0^{r_z} 2\pi J_0(rq_r)\, r\, exp^{(izq_z)}\, drdz \qquad (3)$$

where J_0 is the Bessel function of the zeroth order, r_z is the radius at any point along the Z axis of the cone and the radial component of the q vector $q_r = \sqrt{{q_x}^2 + {q_y}^2}$. Evaluating the integral in the radial direction and assuming constant density within the cones, Equation 3 simplifies to

$$f(q_r, q_z) \propto \int_0^H J_1(r_z q_r) \frac{r_z}{q_r} exp^{(izq_z)}\, dz \qquad (4)$$

where J_1 is the Bessel function of the first order. To fit the experimental images we numerically calculate Equation 4 and use LMFIT [40], an open source Python implementation of a least squares fitting routine. Note that Equation 4 is given in a reference frame fixed to the central axis of the cones which is tilted by γ with respect to the fixed coordinates of the detector. The detector coordinate system (Fourier space) and the cone coordinate system (real space) can be converted from one to the other by a rotation about the y-axis by the angle γ. The tilt angle γ and the cone half opening angle β are included as fitting parameters. Because there is a direct correlation between the angles β and γ, they must be refined iteratively.

Fitting a series of images with a sequence of tilt angles ($25° < \gamma > 45°$) for each sample enables us to determine any possible small offset in the tilt angle γ which may have been introduced during the initial alignment of the sample with the X-ray beam. Because our cones are three dimensional, it is possible there may also be a small misalignment of the sample in the plane orthogonal to the plane of γ rotation. This is modelled as an additional tilt angle fitting parameter ψ. The cone parameters H, R and β are related by

$$R = H \tan \beta \qquad (5)$$

For each sample measured, an average value was determined for the parameters extracted over the whole tilt sequence, and the standard deviation from these measurements is used to provide an estimate of the error for that data point.

As apparent from the right column in Fig. 3, the fits reproduce the experimental data very well, including the fine secondary features between the large streaks. There are some minor differences between the experimental images and the calculated fits. The experimental images appear to be slightly less clear than the calculated fits, most likely due to a narrow size distribution in the conical etch pits, which is not modelled. The experimental images also contain artifacts such as the shadow of the X-ray beam stop and some lines which are generated by inelastic scattering from the crystal planes of the silicon substrate. Naturally, these are not reproduced by the fit.

3. Results and discussion

Figures 5 and 6 show the results from the analysis of the SAXS measurements for all samples irradiated and subsequently etched in 2.5% HF (Fig. 5) and 5% HF (Fig. 6). For successful track etching, it is

necessary that the track etch rate exceeds that of the isotropic bulk etch rate. As etching proceeds along the length of the ion track damage, isotropic bulk etching of the material occurs simultaneously, so to deduce the axial etch rate, the bulk etch rate must be accounted for [41]. Figures 5(a) and 6(a) show the etched depth determined from the measured axial heights, H, of the conical etch pits as a function of etching time. For longer etching times once the damaged track region has been removed, the radial etch rate can be used to approximate the bulk etch rate or the bulk etch rate can also be measured directly using SEM or surface profile measurements. We measured the isotropic bulk etch rates for a-SiO_2 directly using a Dektak surface profiler by determining etch step heights for each etchant concentration of 2.5% HF (υ_b = 10±1 nm/min) and 5% HF (υ_b = 20±2 nm/min). An etch stop medium was used (Apiezon wax) to protect part of an un-irradiated sample from etching, and this sample was etched in the same etchant used to etch the ion tracks.

Figures 5(b) and 6(b) are plots of the half cone opening angles (β) measured for each sample. Figures 5(c) and 6(c) show the values for the base cone radii for each sample calculated by Equation 5 using the measured values for the axial etch depths (Figs. 5(a) and 6(a)) and cone half opening angles (Figs. 5(b) and 6(b)). The solid lines in Fig. 5(a), 6(a), 5(c) and 6(c) are linear fits to the SAXS data points. Their slopes yield the axial etch rates υ_a (Fig. 5(a) and 6(a)) and the radial etch rates υ_r (Fig. 5(c) and 6(c)) for the irradiation and etching conditions studied. The error bars for each data point were calculated by obtaining the standard deviation over the whole tilt sequence analysed for each data point. The deduced etching rates are summarised in Table 1. The error values for the etch rates given in the table were obtained from the error returned by the linear fits.

The axial etch rates for all irradiation energies etched with 2.5% HF (Fig. 5(a)) are linear over the range of etch times plotted, and the linear fit intercepts the y-axis close to zero as expected. There is a small difference in the slopes between the three energies, with υ_a (89 MeV) = 56.7±0.8 nm/min, υ_a (185 MeV) = 47.5±1.8 nm/min and υ_a (1.1 GeV) = 42.9±1.4 nm/min, indicating that the higher the irradiation energy, the lower the etch rate in the axial direction. This contradicts the intuitive view that the track etch rate should increase with increasing energy which has persisted since track etching was evaluated using mainly optical techniques in crystalline materials. Singh *et al*. [42], report on the range of swift heavy ions in polycarbonate which they have observed by subsequently etching the ion tracks and measuring their length using optical microscopy. The track etch rates so deduced vary from around 2 to 9 μm/minute and increase with increasing energy loss. Green *et al.* [43] used track etch rates deduced from optical microscopy measurements to identify charged particles from the length of etched fission tracks in minerals. The track etch rates they deduced were dependent upon crystal orientation and were from around 0.2 to 1.2 μm/hour. The axial etch rates we determined in SiO_2 were at least two orders of magnitude lower, the material we used is amorphous, and in our case the

energy loss is constant over the entire layer of interest (in contrast to the mineral measurements in [43]). Thus it is difficult to make a comparison with these studies.

The axial etch rates for samples etched in 5% HF show a linear trend for the lower etching times, but there is a deviation from the linear trend for some samples etched for longer times. The deviation is attributed to significant overlap of the etched tracks which is discussed later. Therefore, the etching rates were deduced from linear fits to only the first three data points for 54, 89 and 185 MeV, with υ_a (54 MeV) = 106.0±1.6 nm/min, υ_a (89 MeV) = 104.0±5.3 nm/min, υ_a (185 MeV) = 105.7±1.0 nm/min. For the 1.1 GeV samples all four data points were used to deduce and axial etching rate of υ_a (1.1 GeV) = 93.2±3.0 nm/min, since the irradiation fluence was lower (5 x 10^8 ions cm^{-2}) and pore overlapping was not significant. The axial etching rate deduced for the 1.1 GeV samples was significantly lower (slightly more than 10%) than for all of the other energy values. The difference between the axial etch rates for 54, 89 and 185 MeV irradiated samples is within 2 nm/min, which is very small. While the 185 MeV irradiated data intercepts the cone height axis close to zero, both the 1.1 GeV and 89 MeV data are off-set in the negative and positive directions respectively. The intercept value for the 1.1 GeV data obtained from the linear fit is -20.4±16.3 nm, and 99.0±13.9 nm for the 89 MeV data. These off-set values (expected to be zero) highlight the uncertainty in the measurements as well as the limited number of data points.

There is a significant difference in the half cone opening angles between the samples irradiated with 1.1 GeV Au ions and those irradiated with the lower energy ions. For both etchant concentrations the 1.1 GeV samples have a half cone opening angle which is around 20% larger. In the case of samples etched with 2.5% HF, there is minimal difference between the 185 and 89 MeV samples but for samples etched with 5% HF there appears to be a consistent difference between the measured values of β for the three lower energy values with the 185, 89 and 54 MeV samples within 2° of each other, and the values for the 1.1 GeV samples are around 4° higher. This may be related to the so called 'velocity effect': Meftah *et al.* [18] and Toulemonde *et al.* [19] studied the formation of ion tracks under a variety of energy conditions. They concluded that in the electronic stopping regime the spatial energy distribution was of great importance for the formation of ion tracks. For un-etched ion tracks they showed that higher velocity ions induce a larger radial distribution of the energy deposited onto the electronic structure, resulting in a smaller track radius due to the resulting lower radial energy density. This is in also in agreement with [44] where an increase followed by a decrease in the un-etched track radius before the Bragg peak (in Mg_2SiO_4) was predicted by simulation. For the case of etched ion tracks, a decrease in the etched track radius before the ion energy reached the Bragg peak was observed by Jensen *et al.* [45]. Our results could be consistent with these observations because they suggest that despite the higher energy loss of 1.1 GeV compared to 185 MeV and 89 MeV, etching

proceeds more slowly in the direction of the ion track as is evident by the significantly wider cone opening angle and decreased axial etch rate. This suggests that the concentration of defects along the length of the ion track that are attacked by the HF is lower for the higher energy ion irradiation.

The radial etch rates deduced from the plots shown in Figs. 5(c) and 6(c) for both etchant concentrations do not differ significantly from the measured bulk etch rate of a-SiO_2 as expected [41]. For those samples etched in 2.5% HF plotted in Fig. 5(c) there is a small variation in the radial etch rate for the three energies studied. All of the linear fits intercept at a small positive value (6.1±2.9 nm for 1.1 GeV, 4.9±4.2 nm for 185 MeV and 7.4±12.5 nm for 89 MeV). At a bulk etch rate of around 10 nm/minute, these off-set values are significant and are indicative of a non-constant and slightly faster radial etch rate in the vicinity of the radius of the latent ion track damage. These off-set values compare with the values for latent track radii measured by SAXS for 89 and 185 MeV Au ion irradiation published by Kluth *et al.* [28] (For 89 MeV, R = 4.9±1 nm, and for 185 MeV, R = 5.4±1 nm.) For those samples etched in 5% HF there is a very small variation in the radial etch rates deduced of only around 2 nm per minute (see Table 1).

For samples etched with 5% HF the deviation from the linear trend for those data points at higher etching times (for 89 MeV 6 and 8 minutes, for 185 MeV 8 minutes) can be explained by partial overlapping of the etched cones becoming significant. The degree of overlap at a particular track radius is dependent upon the ion fluence and can be calculated using the following formula

$$d = 1 - \exp(-\pi R^2 N) \qquad (6)$$

where d is the area of removed material, R is the radius at the base of the cone, and N is the number of pores. The area of overlap is given by $\pi R^2 N - d$ [36, 46]. The 1.1 GeV irradiations at GSI were performed with a maximum fluence of 5×10^8 ions cm^{-2}. Pore overlapping at this fluence is less than 2%, therefore is not significant at the base cone radii measured. However, for the 185 and 89 MeV irradiations carried out at ANU, a range of irradiation fluences from 2×10^8 to 1×10^{10} ions cm^{-2} was used. The fluence of the 89 MeV sample etched for 8 minutes in 5% HF plotted in Fig. 6 was 1.5×10^9 ions cm^{-2} and the fluence of the 89 MeV sample etched in 5% HF for 6 minutes was 1×10^{10} ions cm^{-2}. These samples were discounted from the etch rate calculations because the degree of overlap at the base of the cones exceeded 30%, adversely affecting their radii measurements. An example of significantly overlapping etched cones is shown in Fig. 7. This image is an SEM micrograph of etched ion tracks in SiO_2 irradiated with 89 MeV Au ions at a fluence of 1.5×10^9 ions cm^{-2} and etched in 5% HF for 8 minutes. The sample is tilted by 15° with respect to the electron beam to highlight the three-dimensional morphology of the overlapping pores. The image shows how the cones are truncated where they overlap, effectively reducing the cone height as well as the cone radii. Although the cones are truncated where they overlap, the cone angles at their base are preserved.

While there is an upper limit for reliable results due to pore overlapping at larger radii, there is also a lower limit due to the small scattering volume of very small cones. Our 2D fitting method could reliably fit cones with radii values as low as around 27 nm. To be able to measure smaller cones using transmission mode SAXS we used higher fluence irradiation to increase the number of scattering objects (and hence the scattering volume) to improve the signal to noise ratio of the images. We also checked the results by fitting the 1D data and comparing the results from both methods. Grazing incidence SAXS (GISAXS) was also used to investigate these very small cones, however the investigation of the small cones is outside the scope of this paper and will be reported on elsewhere.

4. Conclusions

SAXS measurements have been used in conjunction with SEM to characterise conical etched tracks induced by swift heavy ion irradiation and chemical etching under a variety of irradiation and etching conditions. The SAXS technique has allowed us to accurately determine the size and shape of the etched structures with high precision, as we were able to deduce the etch rates in both the axial and radial directions. The results show that at the higher energy of 1.1 GeV, there is a significant difference in the half cone opening angles measured compared with the other lower energies. The axial etch rates also decrease with increasing ion energy. This may be attributed to the velocity effect and the concomitant lower radial energy density at the higher energy. The exact nature of the difference in the density of defects along the length of the ion tracks is still unknown, although from our results it appears to be lower at higher irradiation energy. More work is needed to understand this observation better, and we plan to conduct molecular dynamics simulations to clarify this issue. Because the radial etch rate is limited by the etch rate of the un-irradiated bulk material once outside the vicinity of the ion track damage, the etching behavior in the axial direction is a better indicator of the response of the material to irradiation with swift heavy ions.

Our measurements show that although the size of the etched channels is linear when plotted as a function of etch time, overlapping of the pores for longer etch times can have an effect on the results, as was observed with samples etched with the higher HF concentration of 5% irradiated at ANU. The most consistent set of results was obtained for samples etched with 2.5% HF. From these results it was possible to estimate the radius of the un-etched ion tracks from the y-axis intercepts, which compared well with previous measurements of ion track radii values in SiO_2. Further work is planned to confirm that at shorter etching times the damaged region of the un-etched tracks has an effect on the radial etch rate. To study this in more detail, higher fluence irradiation will be needed to ensure sufficient scattering volume of the resulting very small cones. We have determined the ion track etch rates in both the axial and radial directions for a variety of irradiation and etching conditions in

supported layers of SiO_2. By removal of the Si substrate using standard lithography and anisotropic bulk chemical etching before the irradiation and ion track etching steps, we are now in a position to accurately create conical pores with very narrow openings in free-standing SiO_2, resulting in thin porous membranes with tailored conical nanopores.

5. Acknowledgements

This research is supported by an Australian Government Research Training Program (RTP) Scholarship. The authors also acknowledge financial support from the Australian Research Council and the Australian Synchrotron. Part of the research was undertaken at the SAXS/WAXS beamline at the Australian Synchrotron, part of ANSTO, and we thank the beamline scientists for their technical assistance. Irradiation was conducted at the ANU Heavy Ion Accelerator Facility, and at the GSI Helmholzzentrum für Schwerionenforschung GmbH, Darmstadt, Germany. We thank the ANU HIAF staff for their technical assistance, and we acknowledge the support of our colleagues from the Materials Research Group at GSI. This work was also performed in part at the Canberra node of the Australian National Fabrication Facility, a company established under the National Collaborative Research Infrastructure Strategy (NCRIS) to provide nano and micro-fabrication facilities for Australia's researchers.

References

1. Dekker, C., *Solid-state nanopores.* Nature Nanotechnology, 2007. **2**: p. 209-215.
2. Pérez-Mitta, G., et al., *Highly Sensitive Biosensing with Solid-State Nanopores Displaying Enzymatically Reconfigurable Rectification Properties.* Nano Letters, 2018. **18**(5): p. 3303-3310.
3. Vlassiouk, I., et al., *Versatile ultrathin nanoporous silicon nitride membranes.* Proc Natl Acad Sci U S A, 2009. **106**(50): p. 21039-44.
4. Zhang, Y. and G.C. Schatz, *Conical Nanopores for Efficient Ion Pumping and Desalination.* The Journal of Physical Chemistry Letters, 2017. **8**(13): p. 2842-2848.
5. Fink, D., Petrov, A.V., Hoppe, K., Fahrner, W. R., Papaleo, R.M., Berdinsky, A.S., Chandra, A., Chemseddine, A., Zrineh, A. Biswas, A., Faupel, F., Chadderton, L.T., *Etched ion tracks in silicon oxide and silicon oxynitride as charge injection or extraction channels for novel electronic structures.* Nuclear Instruments and Methods in Physics Research B, 2004. **218**: p. 355-361.
6. Pérez-Mitta, G., et al., *Proton-Gated Rectification Regimes in Nanofluidic Diodes Switched by Chemical Effectors.* Small, 2018. **14**(18): p. 1703144.
7. Venkatesan, B.M.B., R., *Nanopore sensors for nucleic acid analysis.* Nature Nanotechnology, 2011. **6**: p. 615-624.
8. Toimil-Molares, M.E., *Characterization and properties of micro- and nanowires of controlled size, composition, and geometry fabricated by electrodeposition and ion-track technology.* Beilstein J Nanotechnol, 2012. **3**: p. 860-83.
9. Storm, A.J., Chen, J.H., Ling, X.S., Zandbergen, H.W., Dekker, C., *Fabrication of solid-state nanopores with single-nanometre precision.* Nature Materials, 2003. **2**: p. 537-540.
10. Li, J.S., D. McMullan, C. Branton, D. Aziz, M.J. Golovchenko, J.A., *Ion-beam sculpting at nanometre length scales.* Nature, 2001. **412**: p. 166-169.
11. Delalande, M., Cunge, G., Chevolleau, T. Bezard, P., Archambault, S. Joubert, O., Chevalier, X. and Tiron, R., *Development of plasma etching processes to pattern sub-15nm features with PS-b-PMMA block copolymer masks: Application to advanced CMOS technology.* Journal of Vacuum Science and Technology B, 2014. **32**: p. 051086-1-12.
12. Deokhyun, Y., et al., *Improvement of a block co-polymer (PS-b-PMMA)-masked silicon etch profile using a neutral beam.* Nanotechnology, 2016. **27**(38): p. 384002.
13. Andreozzi, A., et al., *The effect of random copolymer on the characteristic dimensions of cylinder-forming PS-b-PMMA thin films.* Nanotechnology, 2011. **22**(18): p. 185304.
14. Apel, P.Y., Korchev, E.Yu., Siwy, Z., Spohr, R., Yoshida, Y., *Diode-like single-ion track membrane prepared by electro-stopping.* Nucl. Instr. and Meth. in Phys. Res. B, 2001. **184**: p. 337-346.
15. Spohr, R., *Method for producing nuclear traces or microholes originating from nuclear traces of an individual ion*, US000004369370A, Editor. 1983, Gesellschaft fur Schwerionenforschung GmbH, Darmstadt, Germany: USA.
16. Young, D.A., *Etching of radiation damage in Lithium Fluoride.* Nature, 1958(4632): p. 375-377.
17. Komarov, F.F., *Nano- and microstructuring of solids by swift heavy ions.* Physics-Uspekhi, 2017. **60**(5): p. 435.
18. Meftah, A., Brisard, B., Costantini, J.M., Dooryhee, E., Hage-Ali, M., Hervieu, M., Stoquert, J.P., Studer, F., Toulemonde, M., *Track formation in SiO_2 quartz and the thermal spike mechanism.* Physical Review B, 1994. **49**(18): p. 12 457-12 463.
19. Toulemonde, M., et al., *Transient thermal processes in heavy ion irradiation of crystalline inorganic insulators.* Nuclear Instruments & Methods in Physics Research Section B-Beam Interactions with Materials and Atoms, 2000. **166**: p. 903-912.
20. Gorbunov, S.A., et al., *Combined model of the material excitation and relaxation in swift heavy ion tracks.* Nuclear Instruments and Methods in Physics Research Section B: Beam Interactions with Materials and Atoms, 2013. **315**: p. 173-178.

21. Lipp, V.P., et al., *Kinetics of propagation of the lattice excitation in a swift heavy ion track.* Nuclear Instruments and Methods in Physics Research Section B: Beam Interactions with Materials and Atoms, 2011. **269**(9): p. 865-868.
22. Orekhov, N.D. and V.V. Stegailov, *Swift heavy ion track formation in nanoporous Si: Wave packet molecular dynamics study.* Journal of Physics: Conference Series, 2018. **946**(1): p. 012026.
23. Mota-Santiago, P., et al., *Nanoscale density variations induced by high energy heavy ions in amorphous silicon nitride and silicon dioxide.* Nanotechnology, 2018. **29**(14): p. 144004.
24. Toulemonde, M., et al., *Synergy of nuclear and electronic energy losses in ion-irradiation processes: The case of vitreous silicon dioxide*. Vol. 83. 2011.
25. Siwy, Z.S., Fulinsky, A., *Fabrication of a Synthetic Nanopore Ion Pump.* Phys. Rev. B, 2002. **89**(19): p. 198103-1 - 198103-4.
26. Trautmann, C., S. Bouffard, and R. Spohr, *Etching threshold for ion tracks in polyimide.* Nuclear Instruments and Methods in Physics Research Section B: Beam Interactions with Materials and Atoms, 1996. **116**(1): p. 429-433.
27. Klaumünzer, S., *Ion tracks in quartz and vitreous silica.* Nuclear Instruments and Methods in Physics Research Section B: Beam Interactions with Materials and Atoms, 2004. **225**(1-2): p. 136-153.
28. Kluth, P., et al., *Fine Structure in Swift Heavy Ion Tracks in Amorphous SiO_2.* Physical Review Letters, 2008. **101**(17).
29. Dallanora, A., et al., *Nanoporous SiO_2/Si thin layers produced by ion track etching: Dependence on the ion energy and criterion for etchability.* Journal of Applied Physics, 2008. **104**(2): p. 024307.
30. Jensen, J., et al., *Ion track formation below 1 MeV/u in thin films of amorphous SiO_2.* Nuclear Instruments & Methods in Physics Research Section B-Beam Interactions with Materials and Atoms, 2006. **243**(1): p. 119-126.
31. Milanez Silva, C., et al., *Processing of nano-holes and pores on SiO_2 thin films by MeV heavy ions.* Nuclear Instruments and Methods in Physics Research Section B: Beam Interactions with Materials and Atoms, 2003. **206**: p. 486-489.
32. Vlasukova, L.A., et al., *Threshold and criterion for ion track etching in SiO_2 layers grown on Si.* Vacuum, 2014. **105**: p. 107-110.
33. Hossain, U.H., et al., *SAXS investigation of un-etched and etched ion tracks in polycarbonate.* Nuclear Instruments and Methods in Physics Research, 2017. **409**.
34. Nadzri, A., et al., *SAXS study on the morphology of etched and un-etched ion tracks in apatite.* Chemical Geology, 2016. **91**: p. 00009.
35. Pepy, G., *New two-dimensional data treatment software for small-angle scattering.* Journal of Applied Crystallography, 2006. **40**: p. s433-s438.
36. Kluth, P., et al., *Measurement of latent tracks in amorphous SiO_2 using small angle X-ray scattering.* Nuclear Instruments and Methods in Physics Research Section B: Beam Interactions with Materials and Atoms, 2008. **266**(12-13): p. 2994-2997.
37. Zeigler, J.F., Biersack, J. P., Littmark, U., *The stopping range of ions in matter*. 1985, New York: Pergammon.
38. Guinier, A., Fournet, G., *Small-Angle Scattering of X-Rays*. 1955, New York, USA: John Wiley & Sons, Inc.
39. Engel, M., et al., *Small-angle X-ray scattering (SAXS) off parallel, cylindrical, well-defined nanopores: from random pore distribution to highly ordered samples.* Applied Physics A, 2009. **97**(1): p. 99-108.
40. Newville, M., Stensitzki, T., Allen, D. B., and Ingargiola, A. *LMFIT: Non-linear least-square minimization and curve-fitting for Python*. 2014 [cited 2018 19 March 2018]; Available from: http://doi.org/10.5281/zenodo.11813.

41. Nikezic, D., Yu, K.N., *Formation and growth of tracks in nuclear track materials.* Materials Science and Engineering R, 2004. **46**: p. 51-123.
42. Singh, M., K. Singh Samra, and R. Singh, *Range and etching behaviour of swift heavy ions in polymers AU - Singh, Lakhwant.* Radiation Effects and Defects in Solids, 2007. **162**(5): p. 333-339.
43. P. F. Green, R.K.B.a.S.A.D., *Particle identification from track-etch rates in minerals.* Nuclear Instruments & Methods, 1978. **157**: p. 185 - 193.
44. Rymzhanov, R.A., et al., *Damage along swift heavy ion trajectory.* Nuclear Instruments and Methods in Physics Research Section B: Beam Interactions with Materials and Atoms, 2019. **440**: p. 25-35.
45. Jensen, J., et al., *Ion tracks in amorphous SiO_2 irradiated with low and high energy heavy ions.* Nuclear Instruments and Methods in Physics Research Section B: Beam Interactions with Materials and Atoms, 2006. **245**(1): p. 269-273.
46. Riedel, C. and R. Spohr, *Statistical properties of etched nuclear tracks.* Radiation Effects, 1979. **42**(1-2): p. 69-75.

Table 1. Irradiation parameters and summary of radial (υ_r) and axial (υ_a) etch rates deduced from the plots shown in Figs 5(a) and 5(c) and Figs 6(a) and 6(c) for the irradiation and etching conditions studied, including energy loss dE/dx values calculated with SRIM2008 [37] and averaged over the thickness of the 2μm SiO_2 layer.

Figure 1. Energy loss of Au ions in a-SiO_2 as a function of ion energy indicating the irradiation energies studied.

Figure 2. SEM micrographs of conical etched pits in SiO_2 irradiated with 185 MeV Au ions and etched with 5% HF for 8 minutes. (a) Cross-sectional view of etched ion tracks in 2 μm thick SiO_2 tilted by 42° with respect to the electron beam, (b) plan view.

Figure 3. Example SAXS γ tilt sequence from γ = 0 to 40° of conical etched pits in SiO_2 irradiated with 1.1 GeV Au ions etched with 2.5% HF for 8 minutes. The experimentally measured images are shown on the left and their corresponding calculated fits on the right.

Figure 4. Schematic of SAXS measurement geometry showing a cone of height H tilted by angle γ with respect to the incident X-ray beam.

Figure 5. Cone heights (corrected by bulk etch rate of 20 nm/min) (a), half cone opening angles (b) and cone base radii (c) deduced from fits to the SAXS data as a function of etching time for samples irradiated with Au ions at energies of 1.1 GeV, 185 MeV and 89 MeV and etched with 2.5% HF. The lines in (a) and (c) are linear fits to the plotted SAXS data, their slopes yield the axial etch rate v_a (a) and radial etch rate v_r (c) for the irradiation and etching conditions studied. The lines between points in (b) are a guide to the eye. The base radii values in (c) were calculated (using Eq. 5) from the corresponding measured values of H and β plotted in (a) and (b).

Figure 6. Cone heights (corrected by bulk etch rate of 10 nm/min) (a), half cone opening angles (b) and cone base radii values (c) deduced from fits to the SAXS data as a function of etching time for samples irradiated with Au ions at energies of 1.1 GeV, 185, 89 and 54 MeV and etched with 5% HF. The lines in (a) and (c) are linear fits to the plotted SAXS data, their slopes yield the axial etch rate v_a (a) and radial etch rate v_r (c) for the irradiation and etching conditions studied. The lines between points in (b) are a guide to the eye. The base radii values in (c) were calculated (using Eq. 5) from the corresponding measured values of H and β plotted in (a) and (b).

Figure 7. SEM image of conical etched ion tracks tilted by 15° with respect to the electron beam at 50000 X magnification, showing the truncated morphology of overlapping etched cones. The sample was irradiated with 89 MeV Au ions at a fluence of 1 x 10^9 ions cm^{-2} and etched for 8 minutes in 5% HF.

Table 1

Ion Energy (MeV)	Average dE/dx (keV/nm)	Etchant concentration (%)	υ_a (nm/min)	υ_r (nm/min)
1100	22	2.5	42.9±1.4	9.0±0.3
185	16	2.5	47.5±1.8	8.5±0.5
89	11	2.5	56.7±0.8	10.0±1.5
1100	22	5	93.2±2.3	21.2±0.8
185	16	5	105.7±1.02	19.6±0.1
89	11	5	104.0±5.3	19.9±0.5
54	7.5	5	106.0±1.6	17.4±1.6

Figure 1

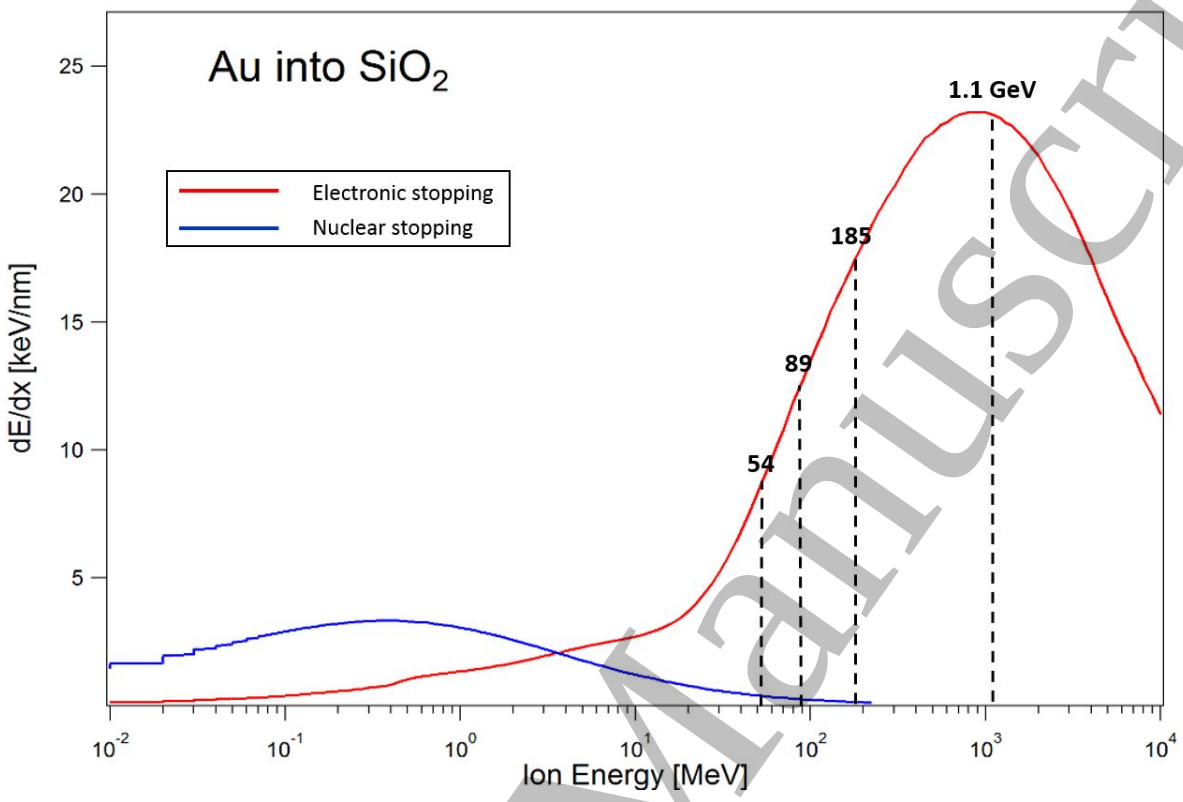

Figure 2

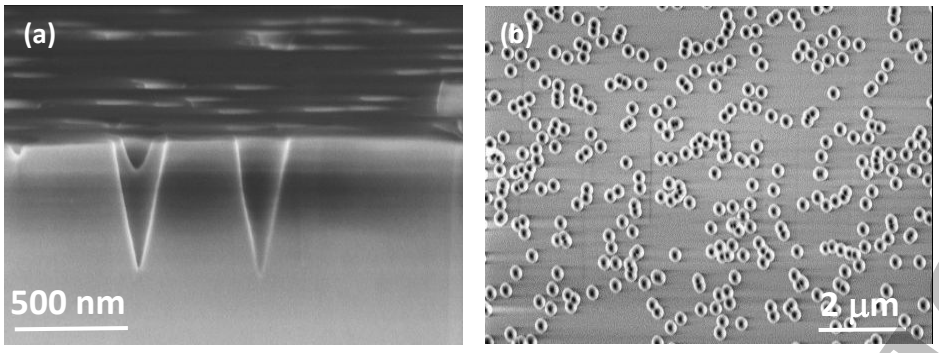

Figure 3

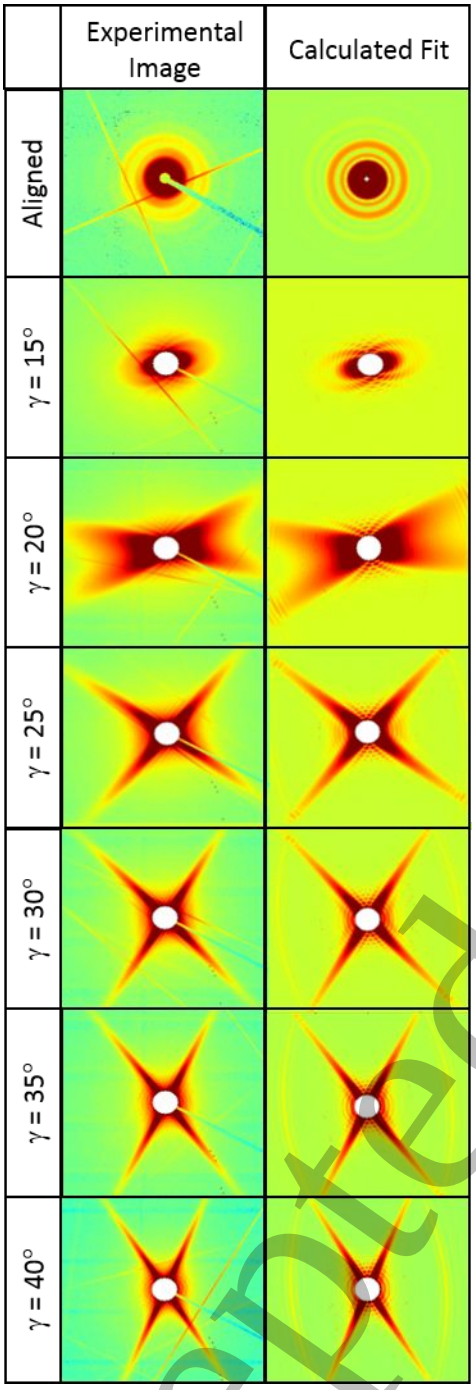

Figure 4

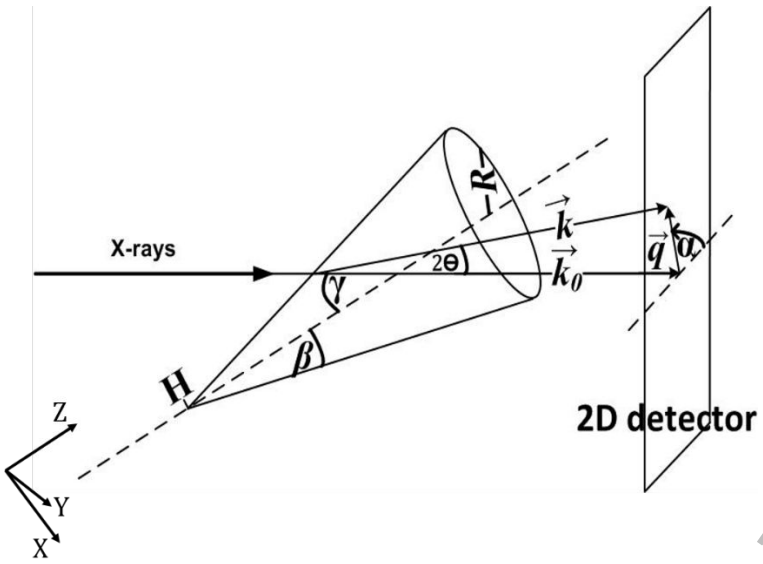

Figure 5

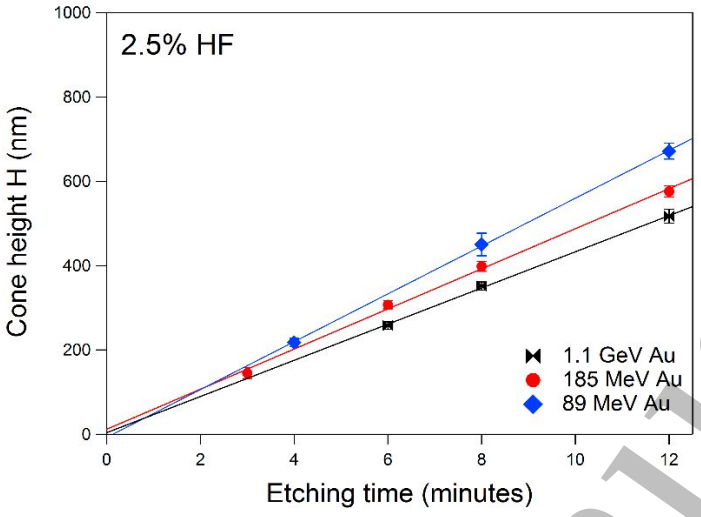

(a)

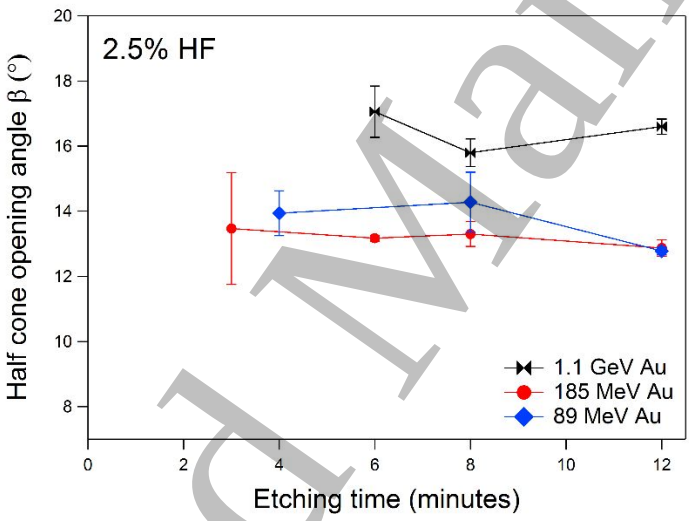

(b)

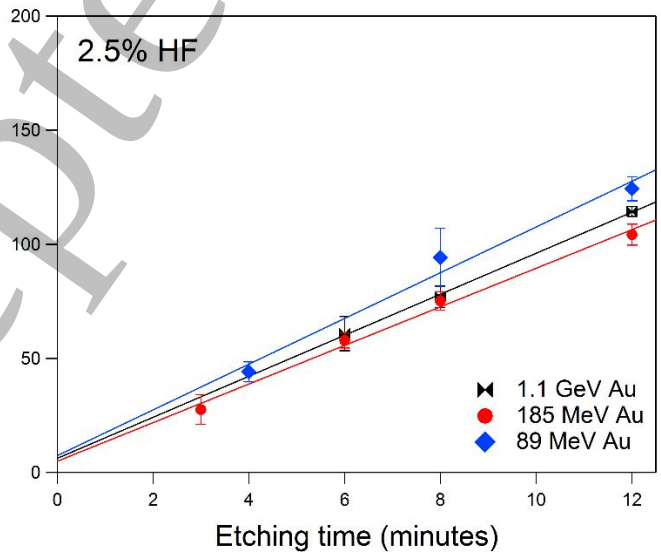

(c)

Figure 6

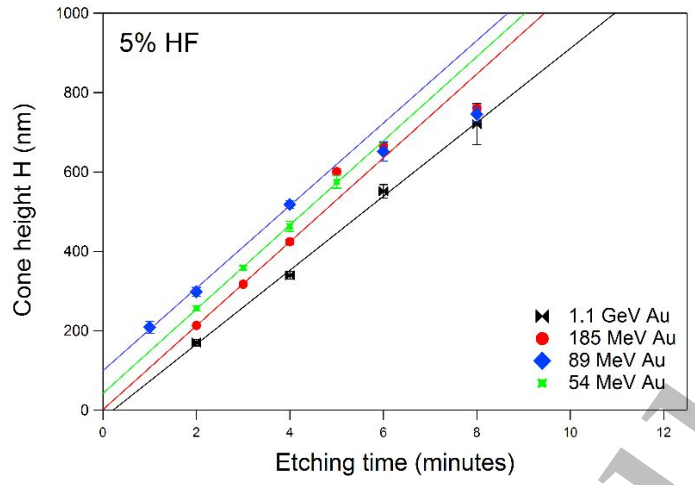

(a)

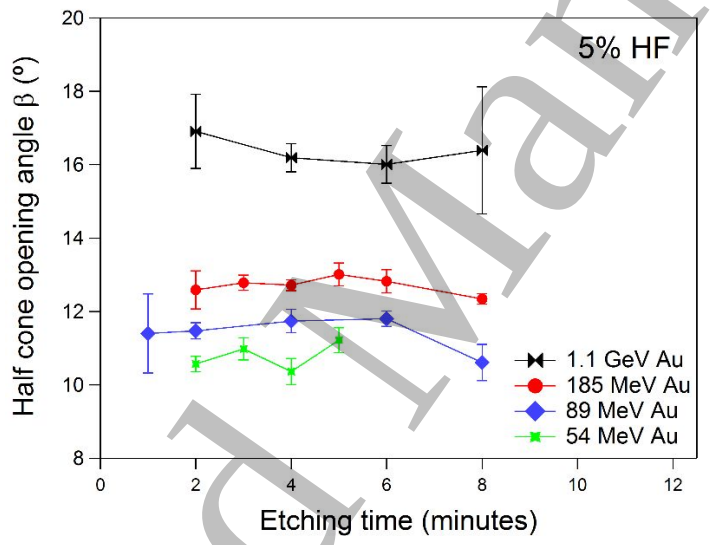

(b)

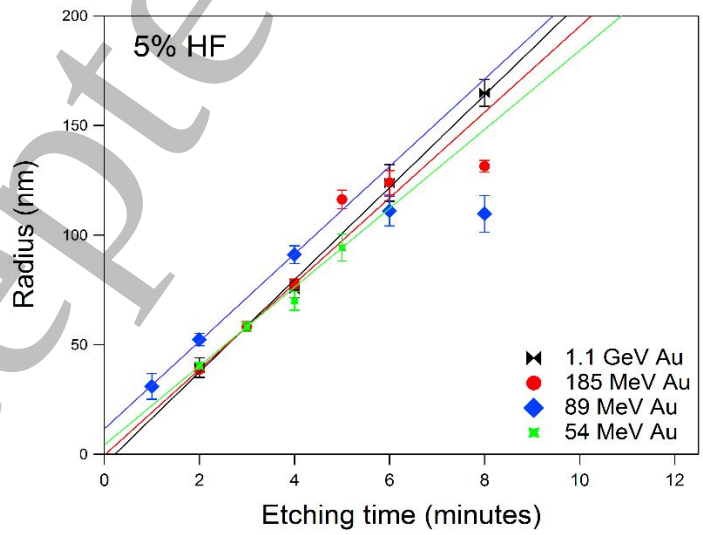

(c)

Figure 7